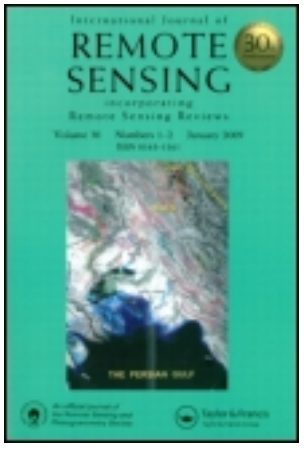

International Journal of Remote Sensing

Publication details, including instructions for authors and subscription information:
http://www.tandfonline.com/loi/tres20

Hot-spot detection and characterization of strombolian activity from MODIS infrared data

D. Coppola[a], M. Laiolo[a], D. Delle Donne[bc], M. Ripepe[c] & C. Cigolini[ad]

[a] Dipartimento di Scienze della Terra, Università di Torino, 10125 Torino, Italy

[b] Dipartimento di Scienze della Terra e del Mare, Università di Palermo, 90123 Palermo, Italy

[c] Dipartimento di Scienze della Terra, Università di Firenze, Firenze, Italy

[d] NatRisk, Centro Interdipartimentale sui Rischi Naturali in Ambiente Montano e Collinare, Università degli Studi di Torino, 10125 Torino, Italy

Published online: 17 Apr 2014.

To cite this article: D. Coppola, M. Laiolo, D. Delle Donne, M. Ripepe & C. Cigolini (2014) Hot-spot detection and characterization of strombolian activity from MODIS infrared data, International Journal of Remote Sensing, 35:9, 3403-3426, DOI: 10.1080/01431161.2014.903354

To link to this article: http://dx.doi.org/10.1080/01431161.2014.903354

International Journal of Remote Sensing, 2014
Vol. 35, No. 9, 3403–3426, http://dx.doi.org/10.1080/01431161.2014.903354

Taylor & Francis
Taylor & Francis Group

Hot-spot detection and characterization of strombolian activity from MODIS infrared data

D. Coppola[a]*, M. Laiolo[a], D. Delle Donne[b,c], M. Ripepe[c], and C. Cigolini[a,d]

[a]*Dipartimento di Scienze della Terra, Università di Torino, 10125 Torino, Italy;* [b]*Dipartimento di Scienze della Terra e del Mare, Università di Palermo, 90123 Palermo, Italy;* [c]*Dipartimento di Scienze della Terra, Università di Firenze, Firenze, Italy;* [d]*NatRisk, Centro Interdipartimentale sui Rischi Naturali in Ambiente Montano e Collinare, Università degli Studi di Torino, 10125 Torino, Italy*

(*Received 28 August 2013; accepted 11 February 2014*)

Identifying and characterizing strombolian activity from space is a challenging task for satellite-based infrared systems. Stromboli volcano is a natural laboratory that offers a unique opportunity for refining thermal remote-sensing applications that involve transient phenomena and small to moderate hot-spots. A new simple and fast algorithm gave us the opportunity to revisit the MODIS-derived thermal output at Stromboli volcano over the last 13 years. The new algorithm includes both night-time and daytime data and shows high performance with the detection of small-amplitude thermal anomalies (<1 MW), as well as a low occurrence of false alerts (<4%). Here, we show that the statistical distribution of volcanic radiative power (*VRP*; in Watts) is consistent with the detection of variable activity regimes that we subdivided into five levels of thermal activity: Very Low (*VRP* < 1 MW), Low (1 MW < *VRP* < 10 MW), Moderate (10 MW < *VRP* < 100 MW), High (100 MW < *VRP* < 1000 MW), and Very High (*VRP* > 1000 MW). The 'Low' and 'Moderate' thermal levels are associated with strombolian activity and reflect fluctuations of the magma level within the conduit feeding the activity at the surface. The 'High' level of thermal output represents the bulk thermal emissions during periods of effusive activity. The highest level ('Very High') was reached only during the onset of flank eruptions (28 December 2002 and 27 February 2007). We found that the retrieved thermal regimes are in general agreement with the explosive levels evaluated at Stromboli since 2005, and their correlation has been shown to be dependent on the observed activity (i.e. eruption onset, lateral flank effusion, summit overflows, strombolian activity). Our results suggest that remotely sensed thermal data provide a reliable tool for monitoring volcanic activity at Stromboli volcano.

1. Introduction

In the last decade thermal remote-sensing techniques have been increasingly applied for monitoring active volcanoes. Ramsey and Harris (2013) give an overview of these applications, discussing the limits of several satellite-based infrared sensors to detect and track volcanic hot-spots. Actually, many of these studies are concentrated on developing near real-time automated techniques, thereby quantifying the heat released and related mass fluxes (Ganci et al. 2012).

A variety of algorithms have been developed for detecting volcanic hot-spots using different satellites and sensors, such as GOES (e.g. Harris et al. 1997), AVHRR (e.g.

*Corresponding author. Email: diego.coppola@unito.it

Harris et al. 1995; Tramutoli 2008), MODIS (e.g. Flynn et al. 2002; Wright et al. 2002), and SEVIRI (Hirn, Di Bartola, and Ferrucci 2009; Ganci et al. 2011). A comprehensive review of these techniques, including their performance and applicability, is given by Steffke and Harris (2011). According to the authors, such algorithms may be subdivided into four main groups on the basis of their detection principles.

(1) *Fixed threshold*, which uses the data on a single pixel to assess whether the radiance or temperature is anomalous (i.e. Flynn et al. 2002; Wright et al. 2002).
(2) *Contextual*, which uses the difference between a pixel's radiance (or temperature) and the surrounding pixels to assess the presence of a hot-spot (i.e. Harris et al. 1995, 2001; Harris, Pilger, and Flynn 2002; Higgins and Harris 1997; Kaneko et al. 2002; Webley et al. 2008; Galindo and Dominguez 2002).
(3) *Temporal*, which compares a pixel's radiance (or temperature) with mean values obtained for the same pixel from time-series of data (i.e. Di Bello et al. 2004; Pergola, Marchese, and Tramutoli 2004).
(4) *Hybrid*, which combines two or more of the above principles (i.e. Dean et al. 1998; Dehn, Dean, and Engle 2000; Kervyn et al. 2006; Hirn, Di Bartola, and Ferrucci 2009; Koeppen, Pilger, and Wright 2011).

In their review, Steffke and Harris (2011) concluded that each algorithm operates well within the limits and criteria of its design requirement. For example, a global detection system such as MODVOLC (Flynn et al. 2002; Wright et al. 2002) has a lower efficiency in detecting hot-spots, but favours the processing of a large amount of data in near real time. On the other hand, the algorithm based on simple temporal principles (i.e. the RST technique of Di Bello et al. (2004)) may be more efficient in detecting local small hot-spots, but requires more complex data processing and is somehow inefficient in providing a continuous record of persistent, stationary thermal anomalies (Koeppen, Pilger, and Wright 2011; Steffke and Harris 2011). The efficiency of any hot-spot detection system may effectively change in regard to the function of the observed volcanic activity. Effusive eruptions can more easily be detected since they represent volcanic targets with high surface temperatures and widespread thermal anomalies (lava flows). Conversely, hot-spot detection over active lava domes is more challenging since these bodies have smaller planar dimensions and cooler lava surfaces (Wright, Glaze, and Baloga 2011). Moreover, the persistence of a thermal anomaly is a further complication for space-based hot-spot detection. For instance, short-lived phenomena (e.g. explosions or short paroxysms) produce transient thermal signals with a small probability of being detected. If these events are associated with small heat emitters (i.e. a volcanic vent and/or vents), they represent critical targets. For these reasons, the detection of 'strombolian activity' from space represents one of the more challenging tasks for satellite-based infrared systems (e.g. Coppola et al. 2012).

Stromboli is an open-system volcano, located in the Aeolian islands (Southern Tyrrhenian Sea; Figure 1), is well known for its persistent volcanic activity and is considered as a reference case for classifying minor to intermediate volcanic eruptions (e.g. Newhall and Self 1982). Volcanic activity is essentially strombolian, with continuous explosions and mild eruptions of scoriae, lapilli, ash, and bombs (Rosi, Bertagnini, and Landi 2000) at summit vents. This activity may be sporadically replaced by lava effusions and more energetic explosions with the eruption of larger volumes of tephra, named 'paroxysms' (Barberi, Rosi, and Sodi 1993).

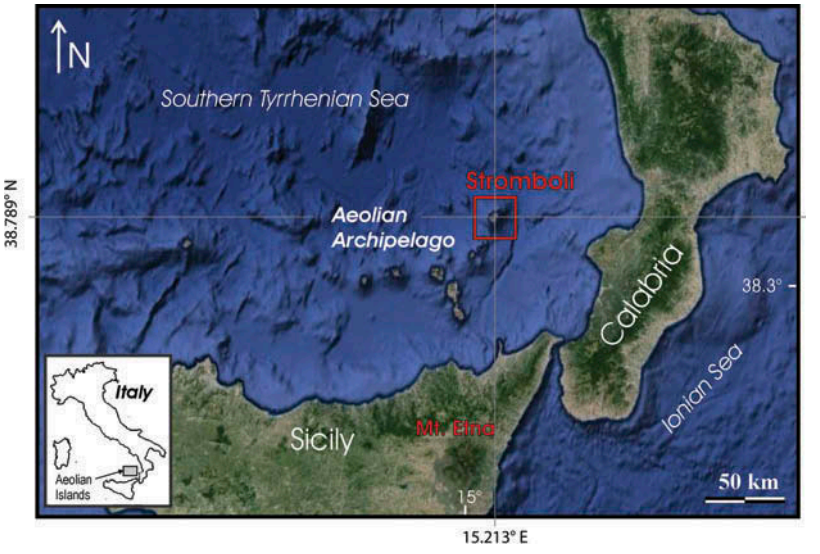

Figure 1. Location of Stromboli volcano in the Southern Tyrrhenian Sea.

At Stromboli, the climate is temperate with maximum temperatures reaching 36–40°C during the summer (July) and minimum temperatures of 0–4°C during winter time (December and January). The rainfall is not abundant and is widely distributed over about 50–90 days per year, with a peak in the cold season. The month with the lowest number of rainy days is July, whereas December and January have the highest number (cf. Laiolo et al. 2012). The sky is clear for 35% of the days in spring, 70% in summer, 50% in the autumn, and 25% in the winter. Snow has rarely been observed at the summit of the volcano (924 m asl). Due to its peculiar volcanic activity and temperate climate, Stromboli volcano may be considered as a natural laboratory for refining infrared remote-sensing applications.

In this article we describe a new algorithm, specifically developed for hot-spot detection at Stromboli volcano. Thus, the algorithm is addressed to detect small thermal anomalies and contains spectral (threshold), spatial (contextual), and temporal principles compatible with the so-called 'hybrid' approach (e.g. Koeppen, Pilger, and Wright 2011). Here, we analyse more than a decade of MODIS data collected on Stromboli by revisiting and updating the earlier analyses of Coppola et al. (2012). After investigating the algorithm performance, we will show how the long-term thermal records may be used to define distinct thermal regimes that characterize the recent activity of Stromboli.

2. The algorithm

The algorithm uses MODIS level 1b data acquired by NASA's Terra (launched in December 1999) and Aqua (launched in May 2002) satellites that normally image Stromboli volcano four times per day (since May 2002). The entire data set (from March 2000 to March 2013), consisting of more than 19,000 images, has been analysed following several main steps. These are: (i) data extraction, (ii) resampling, (iii) definition of regions of interest (ROIs), (iv) hot-spot detection, and (v) calculation of volcanic radiative power (*VRP*).

2.1. Data extraction from MODIS level 1b granules

The first step is dealing with the extraction of data from the MODIS level 1 granules. These data consist of the date and time of satellite overpasses, satellite viewing geometry (zenith and azimuth), the location of each pixel (latitude and longitude), as well as the digital number (DN) related to the spectral bands of interest.

(1) Reflectivity of band 1 (R_1), centred at 0.645 μm (for daytime image only).
(2) Reflectivity of band 2 (R_2), centred at 0.858 μm (for daytime image only).
(3) Radiance of band 6 (L_6), centred at 1.64 μm (for daytime image only).
(4) Radiance of band 21 (L_{21}), centred at 3.959 μm (low-gain MIR channel).
(5) Radiance of band 22 (L_{22}), centred at 3.959 μm (high-gain MIR channel).
(6) Radiance of band 31 (L_{31}), centred at 11.03 μm (TIR channel).
(7) Radiance of band 32 (L_{32}), centred at 12.02 μm (TIR channel).

The DN of each selected band is first scanned to filter out any missed or 'corrupted' datum. According to the MODIS Level 1B Product User's Guide (Toller, Isaacman, and Kuyper 2006), this is achieved by eliminating, for each band, all pixels with DN >32,768 (i.e. invalid data values), with the exception of those with DN = 65,533 (saturated values), used in the subsequent steps.

The georeferenced data are also scanned to remove the bow-tie effect that, at the edge of the swath, produces 'scan to scan' overlapping (Nishihama et al. 1997).

Once the effects of invalid and bow-tie-related pixels have been removed, we use the conversion coefficients for each selected band (scale and offset) in order to convert the DN into reflectivity and/or radiance data (for details regarding this step, see the MODIS Level 1B Product User's Guide).

Finally, we build up a corrected spectral band centred at 3.959 μm (hereby referred to as band L_{21ok}) by using the L_{21} or L_{22} radiance, depending on band 22 saturation (or not), respectively.

2.2. Resampling of original data and production of NTI maps

Cropping and resampling of the original Level 1b MODIS data is necessary for two main reasons, first because high scan angles contribute to the growth of the projected ground spatial element (up to approximately 10 km^2 for scan angles of 55°; Nishihama et al. 1997). This leads the radiance of a potential sub-pixel hot-spot to be integrated over a variable area, thus introducing a further source of error in estimating its thermal output. And second, because the hot-spot detection scheme described below requires an image-to-image registration similar to the application of the RST technique (cf. Di Bello et al. 2004; Pergola, Marchese, and Tramutoli 2004).

Thus, we cropped and resampled (into an equally spaced 1 km grid) the MODIS Level 1b data which fall within a mask (50 km × 50 km) centred over the summit of Stromboli volcano (Figure 2(*a*)). This means that one hot-spot pixel, whose area is 2 km^2 in the original image, becomes two pixels with equal areas of 1 km^2 in the resampled image.

Once the radiances data has been resampled we calculated the normalized thermal index (NTI) for each pixel according to Wright et al. (2002):

$$NTI = \frac{L_{21ok} - L_{32}}{L_{21ok} + L_{32}}. \quad (1)$$

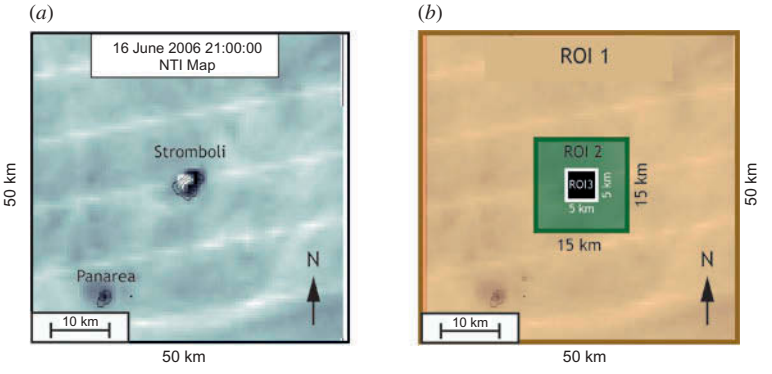

Figure 2. (*a*) Example of NTI Map obtained from night-time images (acquired on 16 June 2006 over Stromboli). Note the thermal anomalous pixels (bright pixels) over the summit of the volcano; (*b*) Regions of interest (ROIs) defined for the hot-spot detection scheme (see text for explanation).

These NTI maps enhance the presence of any sub-pixel hot-spot and represent the reference matrices for subsequent steps of the algorithm.

2.3. *Regions of interest*

A key step in the processing flow chart is the definition of three Regions of interest (ROIs) within the resampled NTI maps. These are centred on the volcano summit (where strombolian activity is taking place) and are normally concentric (see Figure 2(*b*)). ROI_1 consists of an outer ring (50 km × 50 km) and includes the island of Panarea as well as the sea surrounding Stromboli. ROI_2 represents an intermediate region (15 km × 15 km), essentially characterized by the sea surrounding the island of Stromboli. Finally, ROI_3 (5 km × 5 km) samples the island of Stromboli itself, including the coastlines and small portions of its near-shore sea.

2.4. *Hot-spot detection*

The algorithm is based on the characterization of the natural variation of the NTI (seasonal effect) within each ROI. For example, in Figure 2 we plot the NTI time-series relative to the night-time pixels of each ROI during 2006. Note that within this plot, thermally anomalous pixels (hot-spot contaminated) tend to have increased NTI whereas the presence of thick, cold cloud has the opposite effect and tends to lower their relative values (negative spikes).

Seasonal variation in NTI is clear in the three regions, although anomalous pixels are consistent with the presence of hot-spots within ROI_3 (Figure 3(*a*)).

In the following sections we describe the algorithm subdivided for night-time and daytime data, respectively.

2.4.1. *Night-time algorithm*

To detect a hot-spot within the night-time images we first defined two fluctuating thresholds ($NTI_{thresh1}$ and $NTI_{thresh2}$, respectively) that envelop the natural variation of NTI within the whole image (including ROI_1, ROI_2, and ROI_3; Figure 2(*b*)) in the absence of

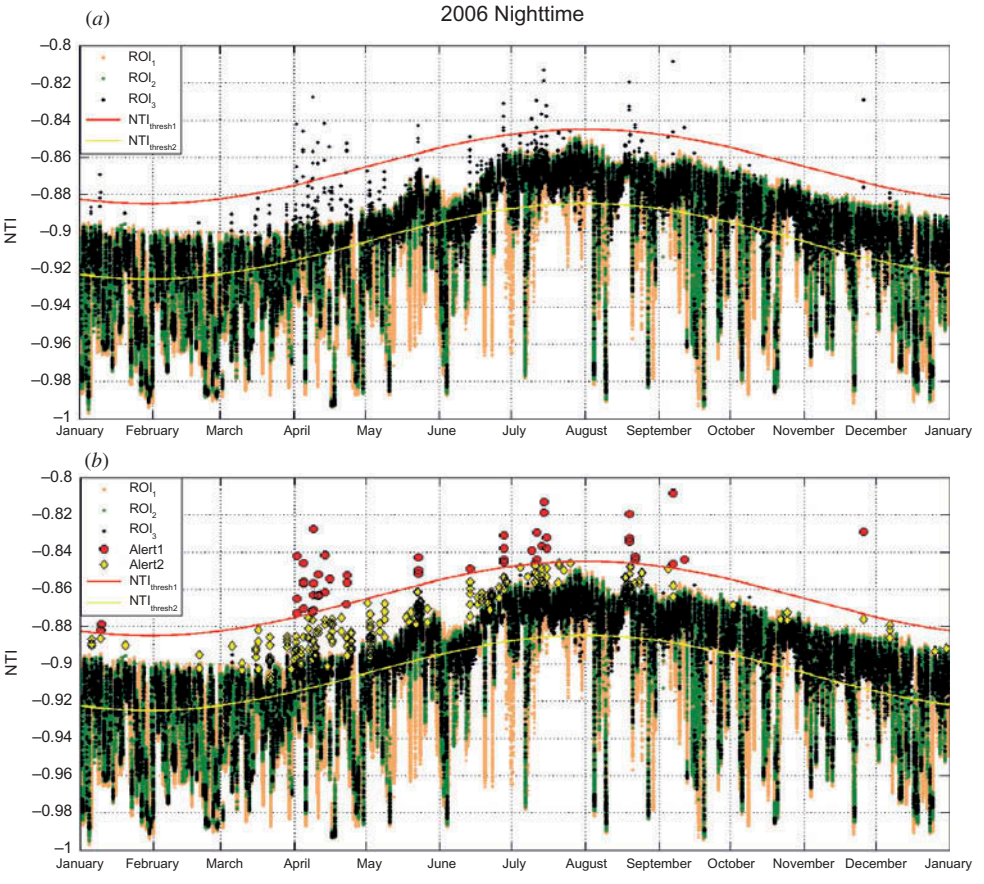

Figure 3. (*a*) NTI time-series for the 2006 night-time data over Stromboli. Each point represents the NTI of a single pixel. Different colours denote the three distinct ROIs (see the electronic text for key to colours). The two sinusoidal lines envelop the fluctuations in NTI due to seasonal trends; (*b*) the same NTI time-series with the alerts detected by the algorithm overlapped. *Alert1* and *Alert2* are obtained using tests 1 and 2, respectively (see the text for explanation).

thermal anomalies and/or cloud cover. These thresholds are obtained by using the form of a typical sinusoidal function which can be described by

$$NTI_{thresh} = A \sin\left[\frac{2\pi}{P}(t-\alpha)\right] + C, \tag{2}$$

where A is the yearly amplitude of NTI variation, P is the length of each cycle (Π/days), t is the time of satellite overpass (julian day), α is the phase shift (i.e. the day when the curve crosses the baseline as it ascend), and C is the baseline, here represented by the average yearly NTI value.

To set the appropriate parameters for the two thresholds (Equation (2)), it is necessary to process at least one year of data. Hence, the operator may chose the appropriate values of A, α, and C by excluding the pixels clearly contaminated by hot-spot and clouds (with

Table 1. Parameters used to define the NTI thresholds (Equation (2)).

Parameter	Unit	$NTI_{thresh1}$	$NTI_{thresh2}$	$NTI_{thresh3}$
A [NTI variation]	adimensional	0.02	0.02	0.07
P [cycle length]	day^{-1}	$\pi/183$	$\pi/183$	$\pi/183$
α [phase shift]	day	121	121	106
C [NTI baseline]	adimensional	−0.865	−0.915	−0.82

NTI values that clearly deviate from the seasonal trend). The values assumed for Stromboli volcano are summarized in Table 1 with their relative NTI thresholds plotted in Figure 3.

These two thresholds define three fields on the NTI time-series, where the upper and lower fields represent the sectors where hot-spot- and cloud-contaminated pixels are surely present

At this point a pixel is considered 'alerted' (hot-spot contaminated) if at least one of the following tests is successfully passed.

The first test is applied to all the pixels of an image (NTI_{ROIS}) and requires that NTI is higher than $NTI_{thresh1}$:

$$Alert1 = NTI_{ROIS} > NTI_{thresh1} \quad (\text{test } 1).$$

The second test is applied for detecting exclusively the smallest thermal anomalies of ROI_3 with an NTI between $NTI_{thresh1}$ and $NTI_{thresh2}$. This is achieved by comparing the NTI of each ROI_3 pixel (not previously alerted by test 1), with some statistical parameters retrieved from a selected suite of 'reference pixels' appertaining to ROI_2. In particular, these reference pixels (NTI_{Ref2}) are the ROI_2 pixels which satisfy the following condition:

$$NTI_{Ref\,2=NTI_{thresh1} > NTI_{ROI2} > NTI_{thresh2}} \quad (\text{condition } 2).$$

Hence according to condition 2, we defined reference pixels as all the pixels of ROI_2 which have NTI between the two thresholds previously defined ($NTI_{thresh1}$ and $NTI_{thresh2}$). In other words, NTI_{Ref2} exclusively includes the pixels surrounding Stromboli volcano that are not contaminated by hot-spots or clouds.

From these reference pixels we thus calculate the maximum value (NTI_{Max2}), mean (NTI_{Mean2}), and standard deviation (NTI_{std2}), which are the parameters used to define the second test:

$$Alert2 = (NTI_{ROI3} > NTI_{Max2}) \text{and } [NTI_{ROI3} > (NTI_{Mean2} + 3 \times NTI_{std2})] \quad (\text{test } 2).$$

Therefore, test 2 determines that a pixel of ROI_3, in order to be considered hot-spot contaminated, must have an NTI higher than that obtained by considering the natural variability of the surrounding region (ROI_2).

The total number of 'alerted' pixels (Alert) is finally obtained by considering all the pixels passing test 1 (Alert 1) or test 2 (Alert 2).

2.4.2. Daytime algorithm

The detection of hot-spot during daytime overpasses is much more complicated, mainly for two reasons, first because radiance in the MIR channel (L_{21ok}) is particularly affected by solar reflection effects (Wright et al. 2002). Solar reflection perturbs NTI as well, especially for pixels sampling reflective surfaces (i.e. water, snow, sand, cloud, etc.), thus causing an increase in its value due to the reflected solar energy (Wright et al. 2002); and second, because during daytime solar heating may effectively enhance the contrast between vegetated and non-vegetated areas. This will produce apparently higher NTI values over volcanic (non-vegetated) areas when compared with the surrounding (vegetated) areas. These intrinsic effects may cause a problematic discrimination of genuine volcanic hot-spots, since during daytime all pixels in non-vegetated areas have NTI values that naturally exceed the surrounding background.

In the attempt to reduce the effects of solar reflection, we apply a correction to L_{21ok} radiance (on the resulting NTI) based on the co-registered radiance recorded on band 6 (L_6). Following Wright et al. (2004) for daytime data, we thus corrected the radiance at 4 μm (L_{21ok}) by subtracting 4.26% of the energy radiated at 1.6 μm (*L6*) (assumed to be the solar reflected component). The corrected NTI thus becomes

$$NTI_{corr} = \frac{(L_{21ok} - (0.0426 * L_6)) - L_{32}}{(L_{21ok} - (0.0426 * L_6)) + L_{32}} \tag{3}$$

Comparison between the uncorrected and corrected NTI, relative to the 2006 daytime data, is shown in Figure 3. In Figure 4(*a*), the uncorrected NTI shows an extremely noisy signal in all ROIs, overprinted on the typical seasonal trend. The noise introduced by solar reflection (represented by spikes) is particularly evident on ROI_1 and ROI_3, both related to the reflective sea surface. On the other hand, the application of Equation (3) (solar correction) produces a clear attenuation of these signals, enhancing the filtered seasonal pattern. Notably, the seasonal trend and the absolute values of the NTI_{corr} relative to ROI_1 and ROI_2 (Figure 4(*b*)) become very similar to those recorded during night-time overpasses (compare Figures 3(*b*) and 4(*b*)). This similarity suggests that the trend recorded by NTI_{corr} is almost exclusively affected by seasonal variation in sea surface temperature (thermal inertia of the sea makes diurnal changes in temperature less pronounced than on land) and increases our confidence that solar contamination has been removed following application of Equation (3).

This is also confirmed by looking at the NTI_{corr} trend of ROI_3, which from April to October (i.e. during the hot season) is 'diverging' from ROI_1 and ROI_2. Such a decoupling can be explained by increase in the temperature gradient occurring between the summit, non-vegetated, volcanic areas (essentially affected by the solar heating), and the surroundings.

We therefore define a single daytime NTI threshold ($NTI_{thresh3}$) that allows us to discriminate between solar heating effects and the presence of a genuine volcanic hot-spot. As previously, we used Equation (2) to describe the seasonal $NTI_{thresh3}$ trend (Figure 4(*b*)). The parameters for calculating $NTI_{thresh3}$ are summarized in Table 1. We thus flag a thermal alert whenever a daytime pixel satisfies the following test:

$$\text{Alert3} = \text{NTI}_{\text{ROIS}} > \text{NTI}_{\text{thresh3}} \quad (\text{test } 3).$$

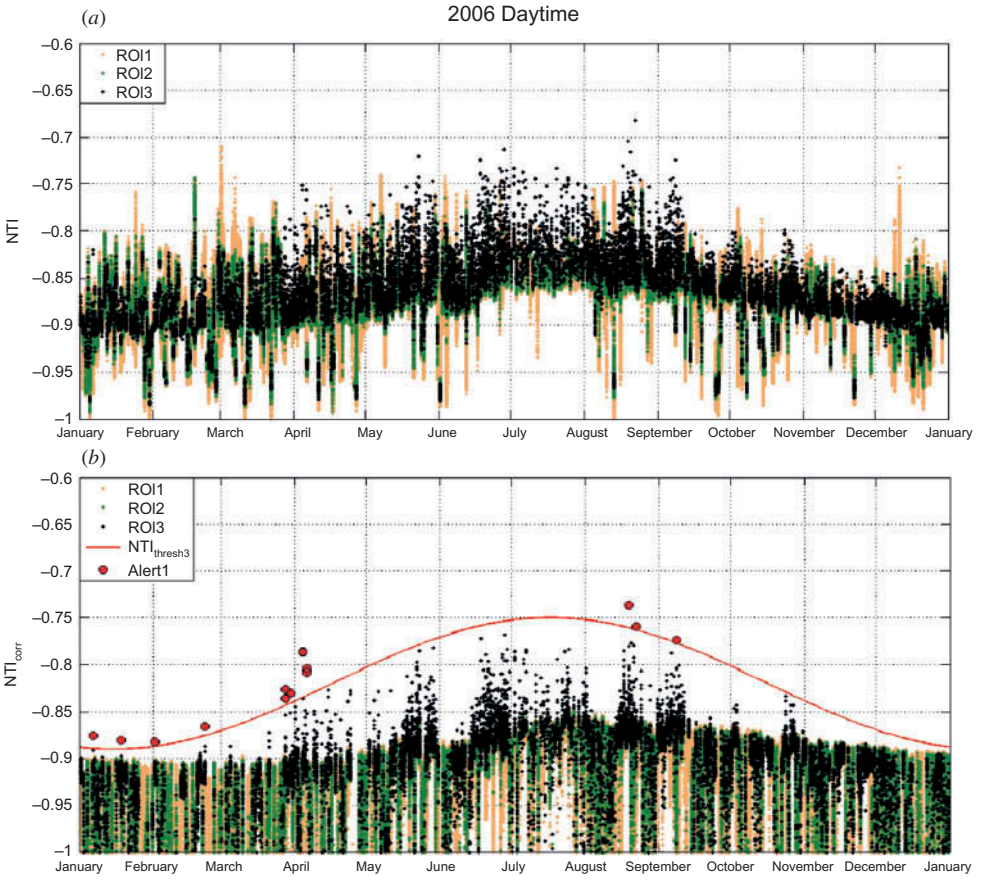

Figure 4. (*a*) NTI time-series relative to the 2006 daytime data over Stromboli. Each point represents the NTI of a pixel. The different colours denote the three distinct ROIs (see the electronic version for colour key); (*b*) NTI time-series corrected for solar reflection according to Equation (3). The alerts detected by the daytime algorithm (obtained using test 3) are overlapped.

As will be discussed later, the capability of detecting hot-spots during daytime is much reduced when compared with the application of the night-time algorithm. This results in poor detection rates during periods of low strombolian activity. However, during periods of more vigorous thermal activity, as well as during effusive eruptions, the results of the daytime algorithm will strongly integrate the dataset recorded during night-time over-passes (cf. Tables 2 and 3).

2.5. *Volcanic radiative power*

When a pixels are flagged as alert, the 'above background' at 4 μm radiance (ΔL_{4PIX}) is calculated as

$$\Delta L_4 PIX = L_{4alert} - L_{4bk} \tag{4}$$

Table 2. Summary of the night-time alerts detected manually ('Manual') and automatically by the Algorithm.

Year	Overpasses no.	Manual[a] no. (%)	Algorithm[a] no. (%)	Correct[1] no. (%)	Missed[1] no. (%)	False[2] no. (%)
2000	339	37 (10.9)	32 (9.4)	25 (67.6)	12 (32.4)	7 (21.8)
2001	406	14 (3.4)	16 (3.9)	10 (71.4)	4 (28.6)	6 (37.5)
2002	597	72 (12.1)	54 (9.0)	50 (69.4)	22 (30.6)	4 (7.4)
2003	818	386 (47.2)	370 (45.2)	364 (94.3)	22 (5.7)	6 (1.6)
2004	833	77 (9.2)	46 (5.5)	45 (58.4)	32 (41.6)	1 (2.2)
2005	836	70 (8.4)	43 (5.1)	39 (55.7)	31 (44.3)	4 (9.3)
2006	819	124 (15.1)	99 (12.1)	91 (73.4)	33 (26.6)	8 (8.1)
2007	822	197 (24.0)	179 (21.8)	175 (88.8)	22 (11.2)	4 (2.2)
2008	827	166 (20.1)	127 (15.4)	125 (75.3)	41 (24.7)	2 (1.6)
2009	835	199 (23.8)	140 (16.8)	140 (70.3)	59 (29.6)	0 (0.00)
2010	836	103 (12.3)	84 (10.0)	83 (80.6)	20 (19.4)	1 (1.2)
2011	837	179 (21.4)	142 (17.0)	138 (77.1)	41 (22.9)	4 (2.8)
2012	830	155 (18.7)	113 (13.6)	110 (71.0)	45 (29.0)	3 (2.6)
TOTAL	9635	1779 (18.5)	1445 (15.0)	1395 (78.4)	384 (21.6)	50 (3.5)

Notes: [a]Percentages are calculated as the number of detections over the number of the overpasses.
[1]Percentages are calculated from the fractions of 'Correct' and 'Missed' detections, with respect to 'Manual' detections.
[2]Percentages are calculated from the fraction of 'False' detections with respect to algorithm detections.

Table 3. Summary of daytime thermal alerts detected by the algorithm.

Year	Overpasses no.	Algorithm no.	Algorithm %[a]
2000	320	3	0.9
2001	397	2	0.5
2002	574	13	2.3
2003	809	172	21.3
2004	813	11	1.4
2005	842	5	0.6
2006	830	11	1.3
2007	836	48	5.7
2008	842	11	1.3
2009	848	27	3.2
2010	821	15	1.8
2011	823	28	3.4
2012	844	18	2.1
TOTAL	9599	364	3.8

Note: [a]Percentages are calculated as the number of detections over the number of the overpasses.

where L_{4alert} is the 4 μm radiance of the alerted pixel/s and L_{4bk} is the background radiance at 4 μm. L_{4bk} is estimated from the arithmetic mean of all pixels surrounding the alerted one (or around the alerted cluster) not contaminated by clouds. Accordingly, cloudy pixels are detected using the method described by Giglio et al. (2003):

$$cloud = [BT_{11} < 255] \quad \text{(condition 4; for night-time data)}$$

or

$$cloud = [(R_1 + R_2) > 0.9]\text{or}[BT_{11} < 245]\text{or}[((R_1 + R_2) > 0.9)\text{and}(BT_{11} < 265)] \quad \text{(condition 5; for daytime data)},$$

where BT_{11} is the brightness temperature (in K) of band 11 (retrieved from L_{11} using Plank's function), and R_1 and R_2 are the reflectivity of bands 1 and 2, respectively.

Following Wooster, Zhukov, and Oertel (2003), we calculated the volcanic radiative power (*VRP* in W) by means of the MIR method. Hence, for any individual alerted pixels, VRP_{PIX} is calculated as

$$VRP_{PIX} = 18.9 \times A_{PIX} \times \Delta L_{4PIX} \tag{5}$$

where A_{PIX} is the pixel size (1 km^2 for the resampled MODIS pixels).

When two or more pixels (a cluster of pixels) are alerted, total radiative power is finally calculated as the sum of the single VRP_{PIX}:

$$VRP = \sum_{1}^{nalert} VRP_{PIX} \tag{6}$$

where *nalert* is the number of alerted pixels.

3. Algorithm performance

Due to the differences between night-time and daytime alert detection procedures, the two algorithms must be considered separately when testing their performance.

To test the performance of the night-time algorithm, we followed the methodology of Steffke and Harris (2011) and we visually inspected all NTI images in order to identify the presence of a real hot-spot ('Manual' alerts, Table 2). These hand-picked images were used as a reference benchmark for comparing these results with those obtained by using the algorithm (see algorithm alerts in Table 2). This is computed in terms of how many automatic detections are effectively consistent with those manually identified (cf. 'Correct' in Table 2). Hence, the difference between the 'Manual' and the 'Correct' detections represents 'Missed' detections (Table 2). Finally, when the algorithm detected a hot-spot that was not validated by visual inspection, we classified it as a 'False' detection (cf. Table 2).

The results of this comparison are shown in Table 2, where the total number of detections (and their relative percentage) are subdivided year by year. In addition, in Figure 5 we also show a typical NTI map for each detection case (Correct, Missed, and False detections).

Overall comparison suggests that the night-time algorithm performs correctly in ~79% of 'Manual' detections, with ~22% of 'Missed' cases and less than 4% of 'False' alerts (Table 2). Notably, all the 'False' detections consist of small-amplitude thermal anomalies (i.e. *VRP* <2 MW), and they could be easily eliminated by setting a cutoff at 2 MW. However, such a cutoff will also produce a strong reduction of the efficiency of the algorithm, with the 'Correct' detections decreasing from ~79% to less than 59%. Since most of the 'False' detections are low-amplitude ones, we preferred to keep some false alerts than missing several real hot-spots.

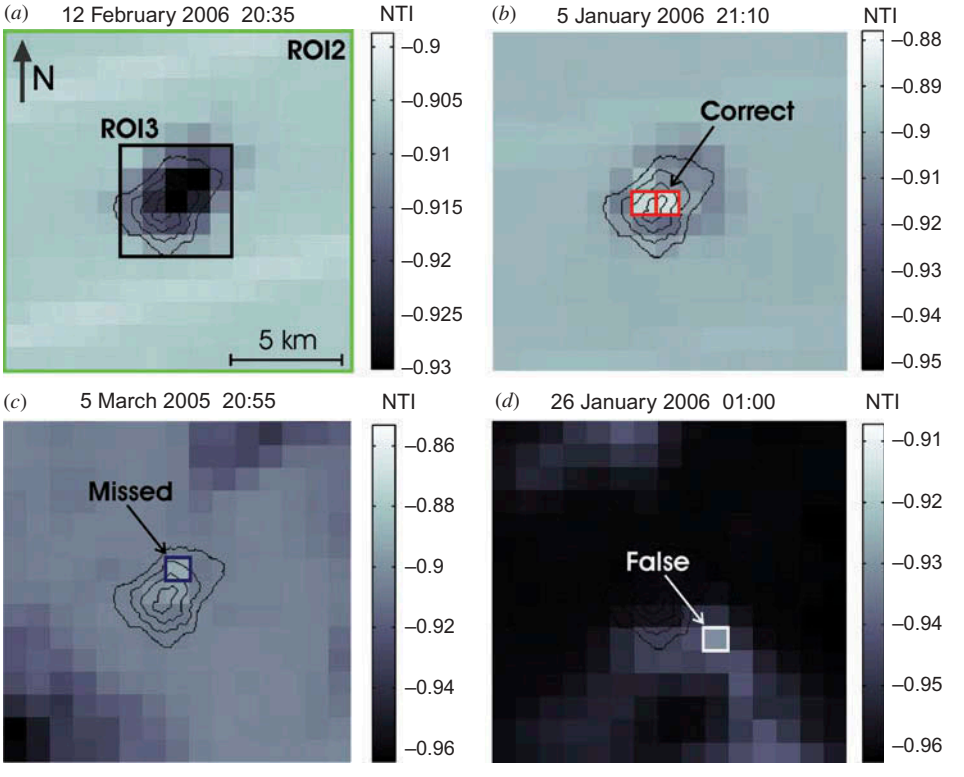

Figure 5. (*a*) Zoomed view of selected night-time NTI map (ROI_2 and ROI_3 only) recorded on 12 February 2006; any anomaly visible over Stromboli volcano and the island appears cooler than the surrounding area. Three other examples of night-time NTI maps represent the following cases: Correct (*b*), Missed (*c*), and False (*d*) detections (resulting from the night-time algorithm). The squares mark the locations of the Correct (red), Missed (blue), and False (white) pixels.

The excellent performance of the night-time algorithm is also evident from comparison of the frequency of alerted detections retrieved both manually ($f_{alertManual} = N_{alert,Manual}/N_{Overpasses}$) and automatically ($f_{alert,algorithm} = N_{alert,,algorithm}/N_{Overpasses}$) (Figure 6(*a*)). The best linear fit plots close to the 1:1 ratio (with $R^2 = 0.97$), suggesting excellent agreement over the whole range of f_{alert}. However, the percentage of 'Correct' detections seems to be affected by the level of volcanic activity (Figure 6(*b*)), which is basically correlated with the frequency of detection ($f_{alert,algorithm}$). This means that the algorithm is most efficient during effusive phases, whereas it is lower during periods of weak to moderate strombolian activity. From Table 2 it is evident that the number of 'False' detections it is not correlated with the level of activity and remains typically around four cases per year.

The overall effectiveness of the night-time algorithm can finally be compared with the results obtained by Coppola et al. (2012), which analysed night-time MODIS data at Stromboli volcano between 2000 and 2012 with a different algorithm. In our previous article (Coppola et al. 2012), we found 743 alerts during 9635 overpasses, with an average frequency of alert detection ($f_{alert} = N_{alert}/N_{Overpasses}$) of 8.5%. Over the same period the new algorithm (Section 2.4.1) detected 1332 alerts (f_{alert} = 15%; Table 2), thus doubling

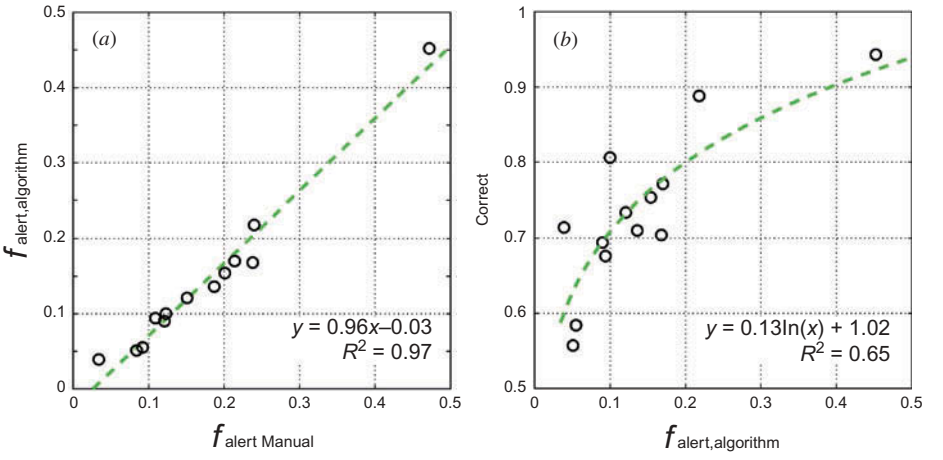

Figure 6. (*a*) Relationship between the frequency of alert detection retrieved manually ($f_{alertManual}$) and automatically ($f_{alert,algorithm}$); (*b*) percentage of 'Correct' detection as a function of $f_{alert,algorithm}$. The algorithm performs almost optimally during the period characterized by $f_{alert,algorithm}$ >0.5.

the detection capability (particularly for small-amplitude thermal anomalies) with respect to our previous algorithm (Coppola et al. 2012). For comparison, during 2000–2012 at Stromboli volcano, the MODVOLC system (which uses a simple fixed threshold) detected 442 night-time alerts (f_{alert} = 4.5%), half of these being identified during effusive periods of activity.

Testing the performance of the daytime algorithm is more problematic, due to the difficulty in discriminating 'false' and 'real' hot-spots using visual inspection of each image. As previously discussed, this difficulty arises from solar heating effects, so that discriminating a genuine volcanic hot-spot from a pixel 'naturally' hotter than its surroundings is somewhat challenging. This is particularly true for low-amplitude thermal anomalies, whose radiance in the MIR channel may exceed their background values to a moderate degree. Therefore, there are no effective benchmarks for testing the daytime algorithm despite visual data inspection. However, this procedure is useful by visual exclusion of the presence of evident 'False' detections.

An alternative approach to evaluate the daytime algorithm takes into account the night-time detections as a reference thermal signal. We thus plotted separately the *VRP* retrieved from night-time and daytime data (Figure 7). In particular, we compared the results for a period of high thermal emissions (the first seven months of effusive activity in 2003; Figure 7(*a*)) with those obtained for one year of lower thermal emissions (characterized by low to mild strombolian activity during 2009; Figure 7(*b*)). In both the cases, the trends of thermal outputs confirm an excellent agreement between the two datasets (daytime and night-time). Notably, during the effusive phase the daytime algorithm performed very well in terms of mean *VRP* (the average value of *VRP* measurements), as well as in tracking the general trend of the eruptive sequence (Figure 7(*a*)). However, the number of daytime detections was almost half that of night-time detections, probably due to the lower efficiency of the algorithm in detecting small thermal anomalies.

The lower sensitivity of the daytime algorithm is also evident by comparing the dataset recorded during one year of typical strombolian activity (i.e. 2009; Figure 7(*b*)).

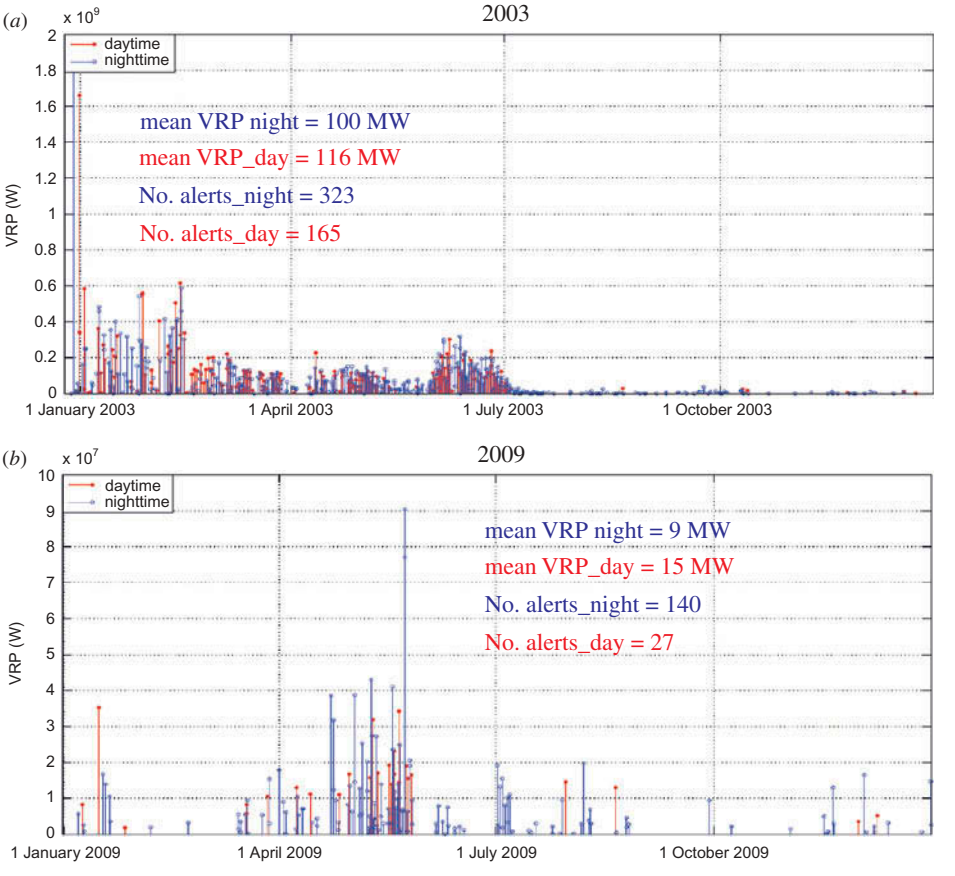

Figure 7. Comparison of thermal outputs during 2003 (*a*) and 2009 (*b*); the night-time algorithm (blue) and the daytime algorithm (red) are reported.

The general trend of daytime data is still consistent with the fluctuations of thermal outputs recorded during night-time. However, the number of alert detections obtained by applying the daytime algorithm drastically decreased. Again these results demonstrate the limits of the daytime algorithm, which is unable to detect smaller hot-spots. In fact the daytime dataset consist of 364 alerts over a total of 9599 overpasses, which gives a mean f_{alert} of 4% (Table 3). This compares with a frequency of alert detection of 15% for night-time images, thus enhancing the difference in efficiency of hot-spot detection between the two algorithms.

4. Statistical analysis of *VRP* and thermal regimes

We here focus our analysis on the night-time dataset for statistical reasons. This dataset consists of a large number of observations (1445 data) and shows a higher efficiency in detecting small thermal anomalies.

As a whole, the entire night-time dataset indicates that *VRP* ranges from <1 MW to more than 3000 MW, thus spanning over three orders of magnitude. Particularly, its

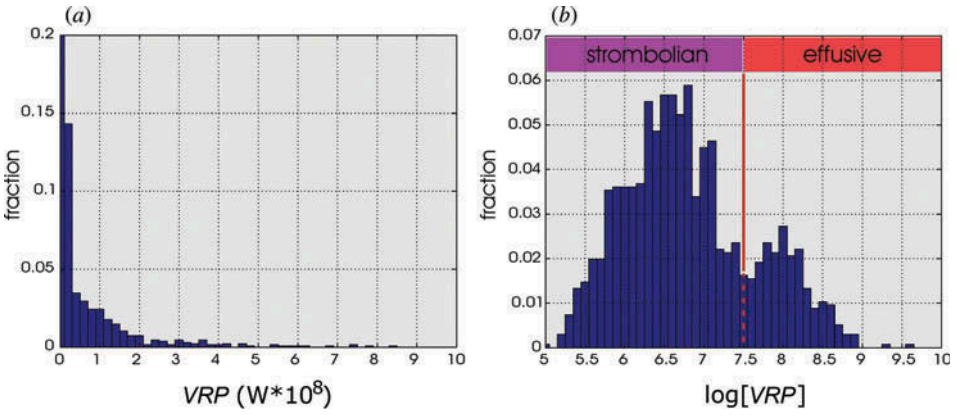

Figure 8. (*a*) Frequency histogram of *VRP* data recorded during 2000–2013 (night-time only); (*b*) frequency histogram of log-transformed data log[*VRP*] enhancing the presence of two main regimes associated with strombolian and effusive activity, respectively. These two regimes intersect at about 30 MW (log[*VRP*]= 7.5).

frequency distribution is extremely peaked and skewed toward higher values, as shown in Figure 8(*a*). A useful way to visualize the shape and properties of such kind of positive, asymmetric distributions consists in transforming the original data (*VRP*) into log-transformed data (log[*VRP*]). This procedure was previously used to identify distinct thermal regimes at Stromboli and Nyamuragira volcanoes (Coppola et al. 2012, Coppola and Cigolini 2013).

Our new dataset for Stromboli volcano (log[*VRP*] records) reveals the presence of two main regimes that intersect around 30 MW (log*VRP* = 7.5; Figure 8(*b*)). Similarly, Coppola et al. (2012) found that a *VRP* of ~50 MW marks a change in the eruptive style of Stromboli, basically identified by the transition from strombolian-dominated to effusive-dominated activity. The small discrepancy between the two thresholds is probably due to the higher sensibility of the new algorithm, which is able to detect a larger number of small thermal anomalies. However our analysis remains consistent with those previously provided by Coppola et al. (2012) and confirms the presence, at Stromboli volcano, of two main thermal regimes (strombolian and effusive) overlapping at 30–50 MW.

Considering the modal value of each regime (the most frequent value), we here estimate that strombolian and effusive activities are characterized by a typical *VRP* of 4 MW (log[*VRP*] = 6.6) and 100 MW (log[*VRP*] = 8), respectively. Based on this simple relation, we may roughly infer that the energy radiated during 25 years of strombolian activity is almost equivalent to that realized during one year of effusive activity.

A closer investigation of *VRP* distribution can be achieved by plotting the log-transformed data (log[*VRP*]) within a normal probability plot (Figure 9). Here, a population of events (or observations) log-normally distributed follows a straight line, as showed by the black dashed line in Figure 8. Although most of the dataset follows approximately this kind of distribution, we suggest that some minor inflection points, separating groups of data, may be regarded as change points indicative of distinct radiating regimes. The inferred inflection points appear around 1, 10, 100, and 1000 MW and define five main radiating regimes hereby named Very Low, Low, Moderate, High, and Very High (Figure 9).

The 'Very Low' radiating regime (*VRP* < 1 MW) represents about 17% of the data and includes essentially most of the false alerts detected by the algorithm. However, in 75% of

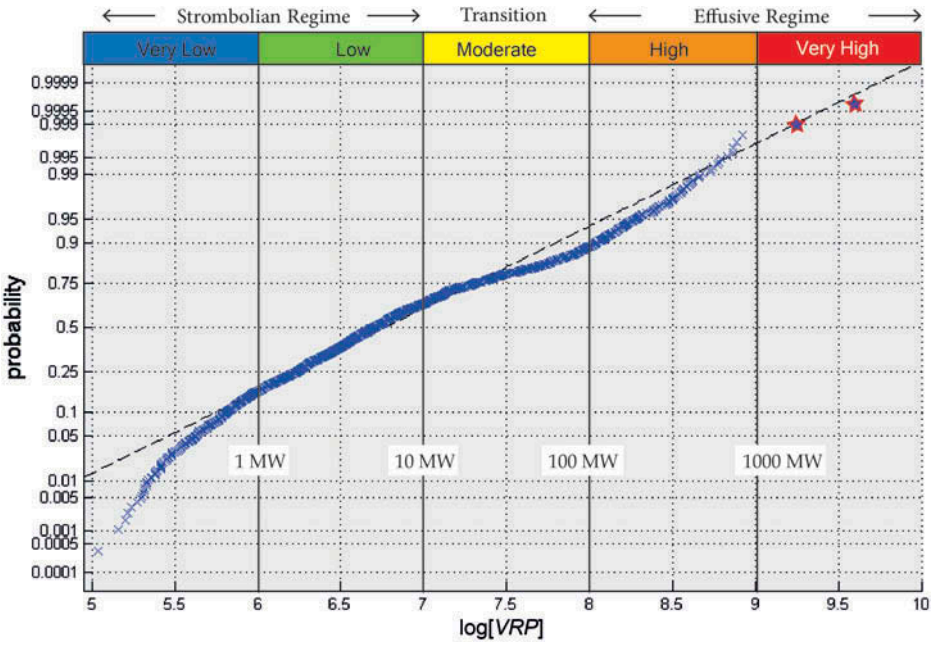

Figure 9. Probability plot of log[*VRP*]. Black dashed line represents the best fit regression by assuming a pure log-normal distribution. The vertical lines represent the inferred inflection points used to define five distinct thermal regimes: Very Low, Low, Moderate, High, and Very High. Note that the two *VRP*s recorded during the onset of the effusive flank eruption (violet stars) are the only 'Very High' values detected between 2000 and 2013. The transition between strombolian- and effusive-dominated activity probably occurs for log[*VRP*] of 30–50 MW in the middle of the Moderate regime.

cases the detection of a Very Low regime represents a genuine hot-spot which may be associated with the presence of a single vent (with a radius of ~1 m and temperature of 950°C) within the summit area of Stromboli.

The 'Low' radiating regime (1 MW <*VRP* <10 MW) is the most represented group, comprising over 47% of the data. This regime consists of bulk thermal emissions associated with the 'typical' strombolian activity typically characterized by persistent degassing and frequent explosive events occurring at one to 15 open vents (Harris and Stevenson 1997).

This regime gradually shifts toward the 'Moderate' radiating regime (10 MW < *VRP* < 100 MW) that is represented by about 25% of the data. The 'Moderate' regime is typical of periods with more vigorous strombolian activity which may evolve into short periods of sustained spattering and/or fountaining, or eventually summit overflows (Coppola et al. 2012). We regard the 'Moderate' regime as a transitional state (between strombolian and effusive) characterized by the uprising of the magma column that feeds the active vents. Eventually this regime may prelude the transition into a pure effusive phase (flank eruption) as observed for a few days before the 2002–2003 and 2007 eruptions (Coppola et al. 2012).

The evolution from 'Moderate' to 'High' thermal regime marks a clear change in the eruptive style of Stromboli, leading to lava effusion (Figure 9). The 'High' radiating regime (100 MW < *VRP* < 1000 MW) is represented by 11% of the data and it has been

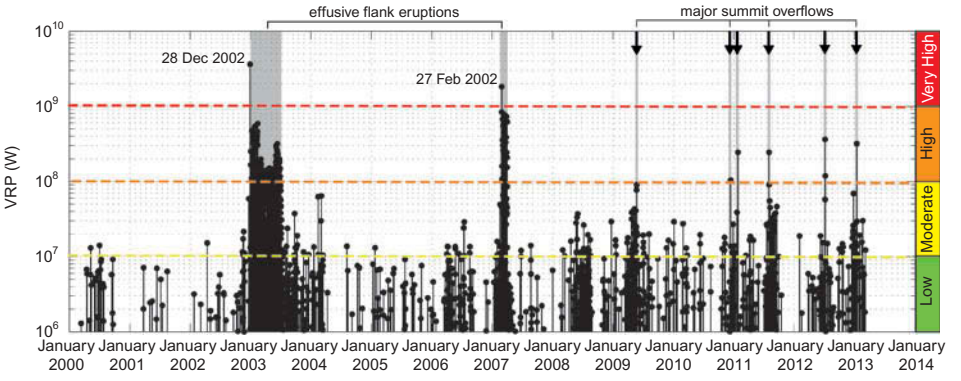

Figure 10. *VRP* time-series (on log scale) recorded at Stromboli between 2000 and 2013. Different colours denote the thermal regimes previously defined (see the text for explanation). Grey bars denote documented periods of effusive activity. The vertical arrows correspond to major summit overflows.

observed exclusively during periods of lava effusion. Included in this regime are two effusive flank eruptions, occurring in 2002–2003 and 2007, as well as all the major summit overflows observed between 2008 and 2012 (black arrows in Figure 10). Periods of mild lava effusion (i.e. <1 m^3 s^{-1}), as for example the second part of the 2002–2003 eruption and the short-lived summit overflows that occurred between 2008 and 2012 (Calvari et al. 2005; Ripepe et al. 2005, INGV Report 2011-08-02), were generally characterized by *VRP* between 100 MW and 400 MW (Figure 10). Conversely, during periods of more vigorous lava effusion (such as the period January to mid-February 2003 and the 2007 eruption), the recorded *VRP* was typically higher than 400 MW, probably in agreement with discharge rates of 1–5 m^3 s^{-1} (Marsella et al. 2009; Calvari et al. 2010).

Finally, the 'Very High' thermal regime (*VRP* >1000 MW) has been recorded only twice during the last 14 years – on 28 December 2002 and 27 February 2007 (Figure 9). In particular, these cases, representing only 0.1% of the data, were recorded a few hours after the beginning of the two major flank eruptions and mark the onset of the main effusive phases. In these cases, lava discharge rates were over 10 m^3 s^{-1} (Calvari et al. 2005; Neri and Lanzafame 2008) and were accompanied the initial and very fast emplacement of lava flows along the 'Sciara del Fuoco'.

Based on this classification, we thus infer that the detection of *VRP* > 100 MW is a clear evidence of ongoing effusive activity at Stromboli volcano. Nonetheless, we also suggest that the detection of a 'Very High' thermal anomaly (*VRP* > 1000 MW) will probably indicate the onset of a new flank eruption.

5. Thermal *versus* explosive levels at Stromboli

The complete time-series of *VRP* recorded between 2000 and 2012 is shown in Figure 10 (night-time data only), with thermal regimes denoted by horizontal dashed lines.

Coppola et al. (2012) reported that all detections above 50 MW were coeval with major episodes of spattering and eventually lava overflows. However, the whole cross-validation of the thermal regimes described above is challenging due to limited field observations and systematic reports. To overcome these problems and to better understand the thermal regimes and their bearing on volcanic activity levels, it is worth comparing

thermal MODIS outputs with the explosive levels recorded (on a daily basis since 2005) by the Laboratorio di Geofisica Sperimentale of the University of Florence (cf. http://lgs.geo.unifi.it/) and sent to the Italian Civil Protection Department (DPC). The explosive level is based on a dataset of several geophysical parameters (seismic, infrasound, number of explosions, deformation) recorded for over a decade: it is subdivided into five levels, representing an average assessment of the explosive intensity (i.e. 0 – Not determined; 1 – Low; 2 – Moderate; 3 – High; 4 – Very high).

The time-series reported in Figure 11 summarizes the thermal and explosive levels (averaged on a weekly basis) recorded between 2005 and 2012, a period that offers an exhaustive example of the variable eruptive styles occurring recently at Stromboli volcano.

For example, during 2005–2006 the activity was typical for Stromboli, with ejection of incandescent ash, lapilli, and scoriae from the summit vents. Although, minor oscillation of the magmatic column has been invoked to explain fluctuating thermal levels (Coppola et al. 2012), there are no records of effusive activity during this time. This almost steady activity was interrupted in February 2007 when a new effusive flank eruption took place. Rapid magma drainage, linked to the opening of a lateral, low-altitude vent, caused the collapse of the central conduit (including the crater area Neri and Lanzafame (2008)) and the sharp cessation of explosive activity at the summit (Ripepe et al. 2009). Lava effusion from the flank persisted for more than one month and was accompanied by a general deflation of the whole volcanic edifice (Bonaccorso et al. 2009). Strombolian activity resumed only 3 months after the end of lava effusion and gradually reached pre-eruptive levels, building new scoria and spattern cones within the collapsed crater area. Different to the pre-2007 eruptive period, between 2008 and 2012 typical strombolian activity was recurrently punctuated by episodic summit overflows, leading to several intra- and extra-crater lava flows (Coppola et al. 2012). These episodes were typically short-lived (from a few hours to several days at most) and were eventually associated with pressurization of the central conduit (Nolesini et al. 2013; Intrieri et al. 2013), coupled with increasing spattering and lava fountaining at the summit vents (Coppola et al. 2012; Smithsonian Institution 2011).

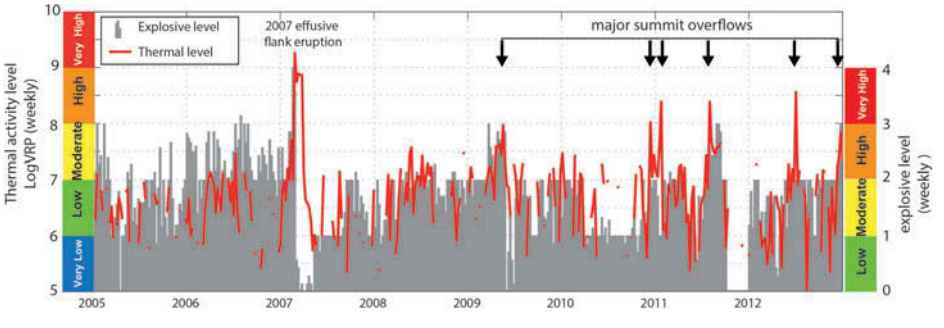

Figure 11. Thermal activity levels (left axis; red line) and explosive levels (right axis; grey bars) recorded between 2005 and 2012. The different colour scales on the two axes denote thermal regimes (obtained by MODIS, left hand-side) and explosive regimes (right hand-side, evaluated by the Laboratorio di Geofisica Sperimentale of University of Florence; http://lgs.geo.unifi.it/) based on multiparametric recordings (seismic, infrasonic, number of explosions, deformation). The black arrows indicate the timing of major summit overflows. The occurrence of the February 2007 eruption is marked by a sharp increase in thermal levels coeval with a decrease in explosive activity.

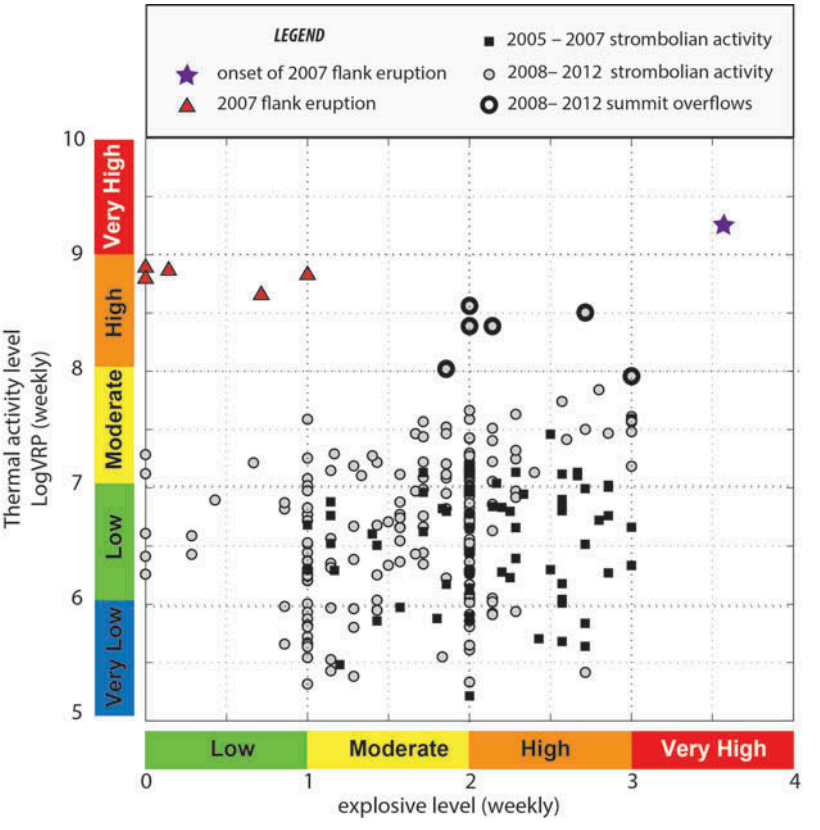

Figure 12. Scatter-plot of explosive *versus* thermal levels of activity recorded at Stromboli between 2005 and 2012. Note how different kinds of activity (shown in the legend) fall within different fields (see text for details).

Although the short-term variations in activity occurring at Stromboli volcano are clearly smoothed on a weekly basis, the comparison shown in Figure 11 suggests that different periods, or different types of activity, show rather peculiar links between thermal and explosive levels.

This is particularly evident by plotting thermal *versus* explosive levels, as shown in Figure 12. Here, several distinct fields may be visualized: each characterizes a specific type of volcanic activity or eruptive period. For instance, the onset of the 2007 effusive eruption (star in Figure 12) was characterized by 'very high' thermal and explosive levels. Conversely, the subsequent flank effusion (red triangles) was characterized by 'high' thermal levels coeval with 'low' explosive activity. As mentioned above, this specific relationship may probably be attributed to the sharp cessation of explosive activity due to the propagation of an effusive fracture down to the central part of the NE flank; this event drained lava out of the crater area, causing high thermal emission and was accompanied by a sharp decrease in geophysical and geochemical parameters (e.g. Ripepe et al. 2009; Cigolini et al. 2013). Conversely, the short-lived effusions associated with summit overflows that occurred between 2008 and 2012 (bold grey circles in Figure 11) are characterized by a different relationship. Here, the 'high' thermal levels, associated with the effusion of lava, are coupled with a 'moderate–high' explosive activity, thus suggesting

that summit outflows are generally accompanied by explosive activity. Field observers effectively reported that during these episodes, intra- and, less frequently, extra-crater lava flows were often associated with increased spattering activity (Smithsonian Institution, 2011), which is in agreement with our thermal versus explosive relationship.

Finally, the whole dataset suggests that the ratio between thermal and explosive levels was somehow different during the 2005–2006 (pre-eruption) and 2008–2012 (post-eruption) periods (black squares and grey circles, respectively). Notably, after the 2007 eruption the thermal level was generally higher than before the eruption, despite the explosive activity fluctuating almost within the same range of levels (Figure 11). In our view, this is a clear indication that the uprising of magma, and its storage at shallow levels, was markedly perturbed by the February 2007 eruption. We thus suggest that the coupled analysis of thermal and explosive levels may provide new insights into the long-term eruptive dynamic of Stromboli volcano.

6. Conclusions

We have developed a new algorithm which specifically addresses the detection of small hot-spots associated with thermal anomalies typical of strombolian activity. In particular, the new algorithm was developed on the basis of the constant siting of thermal anomalies that substantially coincides with the active summit vents. Moreover, it includes principles of contextual, temporal, and spectral hot-spot detection approaches/methods. The application of this algorithm in analysing Stromboli activity is very efficient (up to 95% of correct alerts) and reduces the rate of false alerts (typically around four per year), especially when applied to night-time data. The high efficiency in tracking small hot-spots (<1 MW), coupled with the analysis of MODIS-derived thermal records for over a decade, gave us the opportunity to build up an exhaustive dataset of volcanic radiative power (*VRP*) measurements. Notably, the frequency distribution and probability plot of these thermal records allows the definition of distinct radiating regimes which are closely associated with different levels of volcanic activity. We thus suggest that the implementation of a near real-time processing scheme allow us to discriminate, on the basis of satellite-based thermal monitoring, changes in strombolian activity: such as, for instance, the occurrence of summit overflows and the possible onset of lateral flank eruptions. Finally, we trust that a studious comparison of retrieved thermal outputs to other geophysical and geochemical parameters is an additional key factor for better understanding the eruptive dynamics of Stromboli. Similar approaches could be taken in monitoring other persistently active volcanoes.

Acknowledgements

The manuscript has been improved by the critical comments and suggestions of two anonymous reviewers. We acknowledge NASA-LAADS (http://ladsweb.nascom.nasa.gov/) for providing the complete archive of level 1b MODIS data and the LANCE-MODIS system (http://lance-modis.eosdis.nasa.gov/) for maintaining and delivering Near Real Time MODIS products.

Funding

This research has benefited from funding provided by the Italian Presidenza del Consiglio dei Ministri – Dipartimento della Protezione Civile (DPC) as part of the DEVnet Programme that includes a collaborative project between the Departments of Earth Sciences of the University of Florence and the University of Torino. Scientific papers funded by DPC do not represent its official

opinion and policies. Additional funds for the improving our computing hardware were provided by Fondazione Cassa di Risparmio di Torino (Italy).

References

Barberi, F., M. Rosi, and A. Sodi. 1993. "Volcanic Hazard Assessment at Stromboli Based on Review of Historical Data." *Acta Vulcanologica* 3: 173–187.

Bonaccorso, A., A. Bonfort, S. Gambino, M. Mattia, F. Guglielmino, G. Puglisi, and E. Boschi. 2009. "Insight on Recent Stromboli Eruption Inferred from Terrestrial and Satellite Ground Deformation Measurements." *Journal of Volcanology and Geothermal Research* 182: 172–182.

Calvari, S., L. Lodato, A. Steffke, A. Cristaldi, A. J. L. Harris, L. Spampinato, and E. Boschi. 2010. "The 2007 Stromboli Flank Eruption: Chronology of the Events, and Effusion Rate Measurements from Thermal Images and Satellite Data." *Journal of Geophysical Research* 115 (B4): B04201. doi:10.1029/2009JB006478.

Calvari, S., L. Spampinato, L. Lodato, A. J. L. Harris, M. R. Patrick, J. Dehn, M. R. Burton, and D. Andronico. 2005. "Chronology and Complex Volcanic Processes During the 2002–2003 Flank Eruption at Stromboli Volcano (Italy) Reconstructed from Direct Observations and Surveys with a Handheld Thermal Camera." *Journal of Geophysical Research* 110: B02201. doi:10.1029/2004JB003129.

Cigolini, C., M. Laiolo, G. Ulivieri, D. Coppola, and M. Ripepe. 2013. "Radon Mapping, Automatic Measurements and Extremely High 222Rn Emissions During the 2002–2007 Eruptive Scenarios at Stromboli Volcano." *Journal of Volcanology and Geothermal Research* 264: 49–65.

Coppola, D., and C. Cigolini. 2013. "Thermal Regimes and Effusive Trends at Nyamuragira Volcano (DRC) from MODIS Infrared Data." *Bulletin of Volcanology* 75: 744. doi:10.1007/s00445-013-0744-z.

Coppola, D., D. Piscopo, M. Laiolo, C. Cigolini, D. Delle Donne, and M. Ripepe. 2012. "Radiative Heat Power at Stromboli Volcano During 2000–2011: Twelve Years of MODIS Observations." *Journal of Volcanology and Geothermal Research* 215–216: 48–60.

Dean, K. G., M. Servilla, A. Roach, B. Foster, and K. Engle. 1998. "Satellite Monitoring of Remote Volcanoes Improves Study Efforts in Alaska." *EOS Transactions* 79 (413): 422–423.

Dehn, J., K. G. Dean, and K. Engle. 2000. "Thermal Monitoring of North Pacific Volcanoes from Space." *Geology* 28 (8): 755–758.

Di Bello, G., C. Filizzola, T. Lacava, F. Marchese, N. Pergola, C. Pietrapertosa, S. Piscitelli, I. Scaffidi, and V. Tramutoli. 2004. "Robust Satellite Technique for Volanic and Seismic Hazard Monitoring." *Annals of Geophysics* 47 (1): 49–64.

Flynn, L. P., R. Wright, H. Garbeil, A. J. L. Harris, and E. Pilger. 2002. "A Global Thermal Alert Using MODIS: Initial Results From 2000–2001." *Advances in Environmental Monitoring and Modeling* 1: 5–36.

Galindo, I., and T. Dominguez. 2002. "Near Real-Time Satellite Monitoring During the 1997–2000 Activity of Volcan de Colima (Mexico) and Its Relationship with Seismic Monitoring." *Journal of Volcanology and Geothermal Research* 117: 91–104.

Ganci, G., A. Vicari, A. Cappello, and C. Del Negro. 2012. "An Emergent Strategy for Volcano Hazard Assesment: From Thermal Satellite Monitoring to Lava Flow Modelling." *Remote Sensing of Environments* 119: 197–207.

Ganci, G., A. Vicari, L. Fortuna, and C. Del Negro. 2011. "The HOTSAT Volcano Monitoring System based on Combined Use of SEVIRI and MODIS Multispectral Data." *Annals of Geophysics* 54: 544–550.

Giglio, L., J. Descloitresa, C. O. Justicec, and Y. J. Kaufman. 2003. "An Enhanced Contextual Fire Detection Algorithm for MODIS." *Remote Sensing of Environment*s 87: 273–282.

Harris, A. J. L., L. Keszthelyi, L. P. Flynn, P. J. Mouginis-Mark, C. Thornber, J. Kauahikaua, D. Sherrod, F. Trusdell, M. W. Sawyer, and P. Flament. 1997. "Chronology of the Episode 54 Eruption at Kilauea Volcano, Hawaii, from GOES-9 Satellite Data." *Geophysical Research Letters* 24 (24): 3281–3284.

Harris, A. J. L., E. Pilger, and L. P. Flynn. 2002. "Web-Based Hot Spot Monitoring using GOES: What It Is and How It Works." *Advances in Environmental Monitoring and Modeling* 1 (3): 134–151.

Harris, A. J. L., E. Pilger, H. Garbeil, P. J. Mouginis-Mark, J. Kauahikaua, and C. Thornber. 2001. "Automated, High Temporal Resolution, Thermal Analysis of Kilauea Volcano, Hawaii, using GOES-9 Satellite Data." *International Journal of Remote Sensing* 22 (6): 947–967.

Harris, A. J. L., D. A. Rothery, R. W. Carlton, S. Langaas, and H. Mannstein. 1995. "Non-Zero Saturation of AVHRR Thermal Channels over High Temperature Targets: Evidence from Volcano Data and a Possible Explanation." *International Journal of Remote Sensing* 16 (1): 189–196.

Harris, A. J. L., and D. S. Stevenson. 1997. "Thermal Observations of Degassing Open Conduits and Fumaroles at Stromboli and Vulcano using Remotely Sensed Data." *Journal of Volcanology and Geothermal Research* 76: 175–198.

Higgins, J., and A. J. L. Harris. 1997. "VAST: A Program to Locate and Analyse Volcanic Thermal Anomalies Automatically from Remotely Sensed Data." *Computer and Geosciences* 23 (6): 627–645.

Hirn, B., C. Di Bartola, and F. Ferrucci. 2009. "Combined Use of SEVIRI and MODIS for Detecting, Measuring, and Monitoring Active Lava Flows at Erupting Volcanoes." *IEEE Transactions on Geoscience and Remote Sensing* 47: 2923–2939.

Intrieri, E., F. Di Traglia, C. Del Ventisette, G. Gigli, F. Mugnai, G. Luzi, and N. Casagli. 2013. "Flank Instability of Stromboli Volcano (Aeolian Islands, Southern Italy): Integration of GB-InSAR and Geomorphological Observations." *Geomorphology* 201: 60–69.

INVG Report. 2011. *In Rapporti di Vulcanologia: Sopralluogo a Stromboli del 2 agosto 2011*. http://www.ct.ingv.it/it/comunicati/doc_view/2773-sopralluogo-a-stromboli-del-2-agosto-2011.html

Kaneko, T., A. Yasuda, T. Ishimaru, M. Takagi, M. J. Wooster, and T. Kagiyama. 2002. "Satellite Hot Spot Monitoring of Japanese Volcanoes: A Prototype AVHRR-Based System." *Advances in Environmental Monitoring and Modeling* 1 (1): 125–133.

Kervyn, M., A. J. L. Harris, E. Mbede, F. Belton, P. Jacobs, and G. G. J. Ernst. 2006. "MODLEN: A Semi-Automated Algorithm for Monitoring Small Scale Thermal Activity at Oldoinyo Lengai Volcano Tanzania." Quantitative geology from multiple sources, IAMG annual conference, Liege, September 3–8.

Koeppen, W. C., E. Pilger, and R. Wright. 2011. "Time-series Analysis of Low Resolution Thermal Infrared Thermal Anomalies: A Hybrid Approach." *Bulletin of Volcanology* 73: 577–593. doi:10.1007/s00445-010-0427-y.

Laiolo, M., C. Cigolini, D. Coppola, and D. Piscopo. 2012. "Developments in Real-Time Radon Monitoring at Stromboli Volcano." *Journal of Environmental Radioactivity* 105: 21–29.

Marsella, M., C. Proietti, A. Sonnessa, M. Coltelli, P. Tommasi, and E. Bernardo. 2009. "The Evolution of the Sciara Del Fuoco Subaerial Slope during the 2007 Stromboli Eruption: Relation between Deformation Processes and Effusive Activity." *Journal of Volcanology and Geothermal Research* 182 (3–4): 201–213.

Neri, M., and A. Lanzafame. 2008. "Structural Features of the 2007 Stromboli Eruption." *Journal of Volcanology and Geothermal Research* 182 (3–4): 137–144.

Newhall, C. G., and S. Self. 1982. "The Volcanic Explosivity Index (VEI): An Estimate of Explosive Magnitude for Historical Volcanism." *Journal of Geophysical Research* 87: 1231–1238.

Nishihama, M., R. E. Wolfe, D. Solomon, F. S. Patt, J. Blanchette, A. J. Fleig, and E. Masuoka. 1997. *MODIS Level 1A Earth Location Algorithm Theoretical Basis Document Version 3.0, SDST-092*. Greenbelt, MD: Lab Terrestrial Phys NASA Goddard Space Flight Center.

Nolesini, T., F. Di Traglia, C. Del Ventisette, S. Moretti, and N. Casagli. 2013. "Deformation and Slope Instability on Volcano: Integration of GBInSAR Data and Analog Modeling." *Geomorphology* 180–181: 242–254.

Pergola, N., F. Marchese, and V. Tramutoli. 2004. "Automated Detection of Thermal Features of Active Volcanoes By Means of Infrared AVHRR Records." *Remote Sensing of Environments* 93: 311–327.

Ramsey, M. S., and A. J. L. Harris. 2013. "Volcanology 2020: How Will Thermal Remote Sensing of Volcanic Surface Activity Evolve over the Next Decade?" *Journal of Volcanology and Geothermal Research* 249: 217–233.

Ripepe, M., D. Delle Donne, G. Lacanna, E. Marchetti, and G. Ulivieri. 2009. "The Onset of the 2007 Stromboli Effusive Eruption Recorded by an Integrated Geophysical Network." *Journal of Volcanology and Geothermal Research* 182: 131–136.

Ripepe, M., E. Marchetti, G. Ulivieri, A. J. L. Harris, J. Dehn, M. R. Burton, T. Caltabiano, and G. Salerno. 2005. "Effusive to Explosive Transition during the 2003 Eruption Stromboli Volcano." *Geology* 33 (5): 341–344.

Rosi, M., A. Bertagnini, and P. Landi. 2000. "Onset of Persisting Activity at Stromboli Volcano (Italy)." *Bulletin of Volcanology* 62: 294–300.

Smithsonian Institution. 2011. "*Stromboli.*" *Bullettin of Global Volcanism Program* 36 (9): 5–8. http://www.volcano.si.edu/reports/bulletin/pdf/3609bull.pdf

Steffke, A. M., and A. J. L. Harris. 2011. "A Review of Algorithms for Detecting Volcanic Hot Spots in Satellite Infrared Data." *Bulletin of Volcanology* 73: 1109–1137. doi:10.1007/s00445-011-0487-7.

Toller, G. N., A. Isaacman, and J. Kuyper. 2006. *MODIS Level 1B Product User's Guide*. Greenbelt, MD: Members of the MODIS Characterization Support Team for NASA/Goddard Space Flight Center, 20771.

Tramutoli, V. 2008. "Robust AVHRR Techniques (RAT) for Environmental Monitoring: Theory and Applications." Proceedings of SPIE 3496, earth surface remote sensing II, 101, December 11, 1998. doi:10.1117/12.332714.

Webley, P. W., M. J. Wooster, W. Strauch, J. A. Saballos, K. Dill, P. Stephenson, J. Stephenson, R. Escobar Wolf, and O. Matias. 2008. "Experiences from Real-Time Satellite-Based Volcano Monitoring in Central America: Case Studies at Fuego, Guatemala." *International Journal of Remote Sensing* 29 (22): 6618–6644.

Wooster, M. J., B. Zhukov, and D. Oertel. 2003. "Fire Radiative Energy for Quantitative Study of Biomass Burning: Derivation from the BIRD Experimental Satellite and Comparison to MODIS Fire Products." *Remote Sensing of Environments* 86: 83–107.

Wright, R., L. P. Flynn, H. Garbeil, A. J. L. Harris, and E. Pilger. 2004. "MODVOLC: Near-Real-Time Thermal Monitoring Of Global Volcanism." *Journal of Volcanology and Geothermal Research* 135: 29–49.

Wright, R., L. Glaze, and S. M. Baloga. 2011. "Constraints on Determining the Eruption Style and Composition of Terrestrial Lavas from Space." *Geology* 39: 1127–1130.

Appendix

List of parameters and specific definitions used in the algorithm

Parameter	Definition	Explanation
ROIs	Region of Inerest (s=1,2 or 3)	
NTI	Normalized Thermal Index	Equation (1) applied pixel per pixel on nighttime images
NTI_{corr}	Normalized Thermal Index corrected for solar reflection	Equation (3) applied pixel per pixel on daytime images
NTI_{ROIs}	NTI of pixels within ROIs	Equation (1) applied to the pixels of ROIs
NTI_{Ref2}	Reference pixels of ROI2	Pixels of ROI2 satisfiyng Condition 2
NTI_{Max2}	Maximum NTI of NTI_{Ref2}	
NTI_{Mean2}	Mean NTI of NTI_{Ref2}	
NTI_{Std2}	Standard deviation of NTI_{Ref2}	
NTI_{thres1}	Empirical upper NTI threshold (nighttime algorithm)	Equation (2) with parameters settled in Table 1
NTI_{thres2}	Empirical lower NTI threshold (nighttime algorithm)	Equation (2) with parameters settled in Table 1
NTI_{thres3}	Empirical upper NTI threshold (daytime algorithm)	Equation (2) with parameters settled in Table 1
Alert1	Alerted pixel(s)	Pixel(s) flagged as 'alert' using Test 1 (nighttime algorithm)
Alert2	Alerted pixel(s)	Pixel(s) flagged as 'alert' using Test 2 (nighttime algorithm)
Alert3	Alerted pixel(s)	Pixel(s) flagged as 'alert' using Test 3 (daytime algorithm)
cloud	Cloudy pixel(s)	Pixel(s) considered as 'cloudy' using Conditions 3 and 4
L_{4alert}	MIR radiance (at 4 mm) of alerted pixel (s)	
L_{4bk}	Backgound MIR radiance (at 4 mm) of alerted pixel(s)	arithmetic mean of all the pixels surrounding the alerted one (or around the alerted cluster) not contaminated by clouds
ΔL_{4PIX}	'Above background' MIR radiance of alerted pixel(s)	Equation (4)
VRP_{PIX}	Volcanic Radiative Power of alerted pixel(s)	Equation (5)